



Contents lists available at ScienceDirect

Spectrochimica Acta Part A: Molecular and Biomolecular Spectroscopy

journal homepage: www.elsevier.com/locate/saa

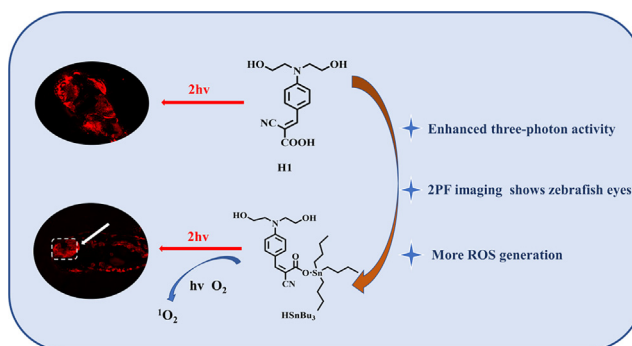
Multi-photon absorption organotin complex for bioimaging and promoting ROS generation

Changting Cai^{a,1}, Mengqi Lv^{b,1}, Pan Xiang^{b,1}, Chengjian Fang^a, Wen Ma^a, Xiaohe Tian^b, Xinsheng Xu^c, Yupeng Tian^a, Qiong Zhang^{a,d,*}^a Department of Chemistry, Key Laboratory of Functional Inorganic Material Chemistry of Anhui Province, Key Laboratory of Structure and Functional Regulation of Hybrid Materials (Anhui University), Ministry of Education, Anhui University, Hefei 230601, PR China^b School of Life Science, Anhui University, Hefei 230601, PR China^c School of Physics and Electronic Information, Anhui Normal University, Wuhu, Anhui 241000, PR China^d State Key Laboratory of Coordination Chemistry, Nanjing University, PR China

HIGHLIGHTS

- The complex (**HSnBu₃**) exhibited three-photon activity.
- Two-photon fluorescence imaging indicated deeper tissue penetration after incubation with **HSnBu₃**.
- **HSnBu₃** could promote ROS generation and induce a decrease in mitochondrial membrane potential after irradiation.

GRAPHICAL ABSTRACT



ARTICLE INFO

Article history:

Received 1 February 2021

Received in revised form 17 April 2021

Accepted 4 May 2021

Available online 18 May 2021

Keywords:

Multi-photon
Organotin complex
Fluorescence imaging
ROS

ABSTRACT

Compared to general fluorescent dyes, multi-photon fluorescent dyes exhibit deeper tissue penetration and lower auto-fluorescence in the bio-imaging field. Therefore, it is necessary to develop an efficient multiphoton imaging agent for deep tissue imaging. In this work, an organotin derivative (**HSnBu₃**) has been designed and synthesized, which shows multiphoton absorption activity. In contrast to the ignorable three-photon activity of the ligand, the complex (**HSnBu₃**) exhibits three-photon activity under NIR excitation (1500 nm). Results of chemical and biological tests confirmed that **HSnBu₃** was more easily activated by oxygen resulting in a higher level of ¹O₂, which could induce a decrease in mitochondrial membrane potential in HepG2 cells. It suggests that **HSnBu₃** has potential in photodynamic therapy.

© 2021 Elsevier B.V. All rights reserved.

1. Introduction

Multi-photon absorption/fluorescence is a nonlinear optical process [1–2]. Among the multi-photon properties, the materials bearing two-photon properties are most widely studied [3–5]. To date, some significant progresses have been demonstrated in developing organic molecules with large three-photon absorption (3PA). A number of methods have been developed to optimize mul-

* Corresponding author.

E-mail address: zhangqiong.314@163.com (Q. Zhang).¹ These authors contributed equally to this work and should be considered co-first authors.

tiphoton systems, including covalent methods for linking the component chromophores [6]. According to reports, these probes with D- π -D, A- π -D- π -A and D- π -A structures, can be excited into the near-infrared region and used for biological imaging [7–13]. However, these probes have the disadvantage of low synthetic efficiency though they can produce arrays with large numbers of chromophores. And it has been reported that some inorganic and organic hybrid complex molecules also have the potential to be used as near-infrared fluorescent probes. For example, Kang Taek Lee et al. reported a pH-responsive nanocomposite based on lanthanide-doped upconverting nanoparticles (UCNPs). Through multiphoton absorption and energy migration between spatially separated Nd³⁺, Yb³⁺, and Tm³⁺ in a three-layered NaYF₄ host coated with FITC (fluorescein-5-isothiocyanate), this nanocomposite can measure the pH with high sensitivity. In addition, three-dimensional imaging of other such nanoparticles has been performed [14–15]. Therefore, it is necessary to try to design and synthesize new materials with enhanced multi-photon absorption by inorganic and organic hybrid methods. Noncovalent methods, such as metal – ligand complex (MLC) based energy transfer systems have received much attention, due to their crystalline nature, and the well determined distances and angles between the units [16]. By varying the metal ligand combination, the binding strength, reversibility, and solubility of the MLCs and thus their optoelectronic properties can be readily tuned [17–19]. Combining the structural diversity and low cost of the organotin carboxylate complexes with multi-photon absorption properties, significantly, it is proposed to develop complexes with multi-photon absorption properties to be applied in biology [20–21]. Organotin (IV) compounds are of large dosages in industry and are considerable in new antibiotic development because of their extensive applications. Organotin complexes show excellent potential as safe anticancer and antimicrobial metal agents [22–23]. In our previous work, several series of two-photon-active organotin complexes were designed and synthesized, these organotin complexes, as fluorescent probes, exhibit not only two-photon activity but also antimicrobial and tumor therapeutic properties [24–25]. However, to the best of our knowledge, the study of three photon absorption based on organotin is rarely reported, which deserved our attention.

Hence, we designed aniline-based organotin (IV) carboxylic acid derivative (**HSnBu₃**) (Fig. 1). Firstly, the aniline group with strong electron donor and good flatness can be used as a building block of the multi-photon chromophore. The carboxyl group not only improves the electron absorption ability, but also enhances the coordination ability [26]. Secondly, CN group with electron-withdrawing ability (Acceptor) is introduced on the π bridge to enhance nonlinear optical properties [27]. Thirdly, compared to our previous work [28], two hydroxyl groups can form hydrogen bonds to increase water solubility, while butyl groups can increase fat-solubility, the bioactivity of complex was enhanced. Also, the complex exhibited excellent two-photon absorption activities rather than the mono-hydroxyl organotin (IV) carboxylic acid complexes [28]. Furthermore, **HSnBu₃** in this work displays excellent three-photon absorption activity in the near-infrared region. Two-photon fluorescence imaging of zebra fish showed that the compound could enter the organism and metabolize separately. Furthermore, both chemical and biological tests revealed that complex (**HSnBu₃**) could produce excessive ROS and induce mitochondrial damage.

2. Experimental section

Q3 [29,30]: N-Phenyldiethanolamine (18.12 g, 0.1 mol) dissolved in pyridine (250 mL) in the flask (500 mL), then Acetic anhy-

dride (25.52 g, 0.25 mol) were added to it. The reaction mixture was refluxed for 24 h. After extraction, it was added to the frozen salt formed by DMF (14.62 g, 0.2 mol) and POCl₃ (61.30 g, 0.4 mol). The reaction mixture was refluxed for 8 h. Stir in ethanol solution with 10% NaOH at room temperature for 24 h. The yellow solid was obtained (15.10 g, yield 71%).

H1: Q3 (2.09 g, 10 mmol) was dissolved in acetonitrile solution (30 mL) in the flask (150 mL), then cyanoacetic acid (1.70 g, 20 mmol) and several drops piperidine were added to it. The reaction mixture was refluxed for 6 h. Resulting mixtures was cooled and filtered. The orange-yellow solid was obtained (1.81 g, yield 87%). IR (KBr, cm⁻¹) selected band: 3577 (vs), 3377 (vs), 2963 (w), 2208 (vs), 1692 (vs), 1611 (vs), 1573 (vs), 1518 (vs), 1479 (w), 1441 (m), 1330 (w), 1191 (vs), 1170 (vs), 1045 (m), 1013 (s), 967 (m), 886 (w), 712 (m). ¹H NMR (*d*₆-DMSO, 400 MHz, ppm) δ 13.31 (s, 1H), 8.04 (s, 1H), 7.90 (d, *J* = 9.2 Hz, 2H), 6.86 (d, *J* = 9.2 Hz, 2H), 3.57 (t, *J* = 4.2 Hz, 6H), 3.36 (s, 2H). ¹³C NMR (*d*₆-DMSO, 100 MHz, ppm) δ 165.2, 153.6, 152.5, 133.7, 118.2, 118.0, 111.7, 93.2, 58.0, 53.0. ESI-MS: calcd: 275.11, found: 275.09.

HSnBu₃: H1 (0.55 g, 2 mmol) and tributyltin oxide (0.6 g, 1 mmol) was dissolved in benzene (30 mL) in the flask (150 mL). The reaction mixture was refluxed for 12 h. The resulting solution was evaporated and was dispersed by diethyl ether. The yellow solid was obtained (0.39 g, yield 71%). IR (KBr, cm⁻¹) selected band: 3384 (vs), 2926 (s), 2211 (vs), 1575 (vs), 1516 (vs), 1480 (w), 1430 (s), 1331 (vs), 1241 (m), 1184 (vs), 1074 (m), 999 (w), 819 (s), 731 (s). ¹H NMR (400 MHz, *d*₆-DMSO) δ 7.86 (s, 1H), 7.80 (d, *J* = 8.8 Hz, 2H), 6.82 (d, *J* = 9.2 Hz, 2H), 4.81 (t, *J* = 5.2 Hz, 2H), 3.66 – 3.45 (m, 9H), 1.60 (dt, *J* = 15.6, 7.6 Hz, 6H), 1.39 – 1.24 (m, 7H), 1.15 – 1.09 (m, 5H), 0.87 (t, *J* = 7.2 Hz, 9H). ¹³C NMR (100 MHz, *d*₆-DMSO) δ 166.5, 152.0, 151.3, 133.1, 120.2, 119.5, 112.1, 100.1, 58.7, 53.8, 28.6, 27.0, 19.5, 14.3. MALDI-TOF: *m/z*, cal.: 566.22, found: 567.09 [M + 1]⁺. ¹¹⁹Sn-NMR (*d*₆-DMSO): δ = -25.21 ppm.

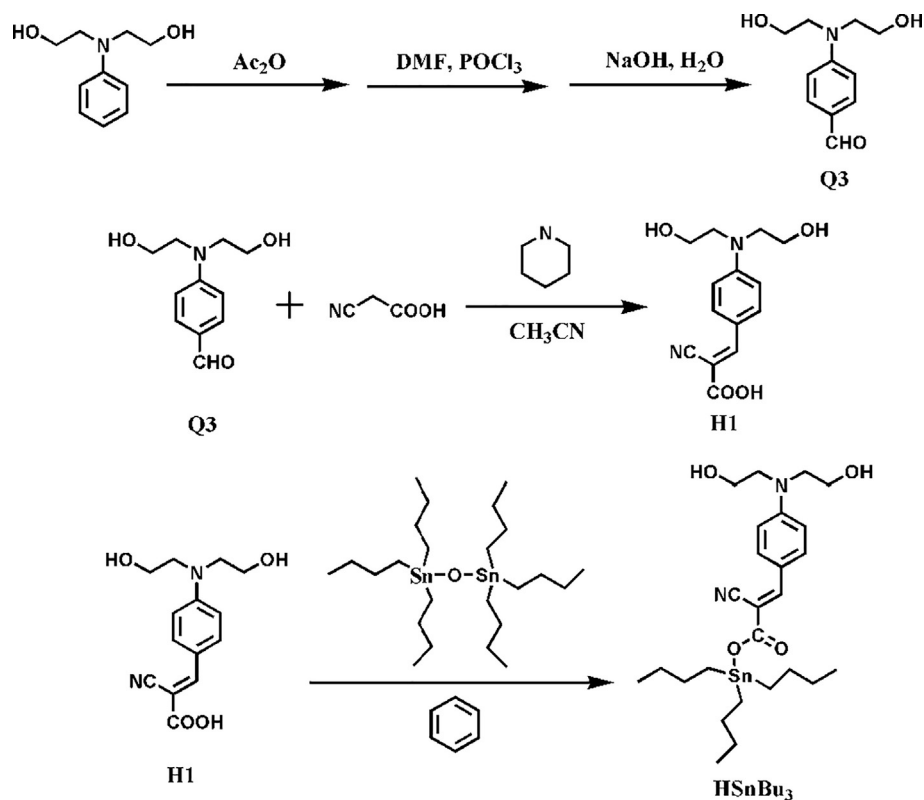
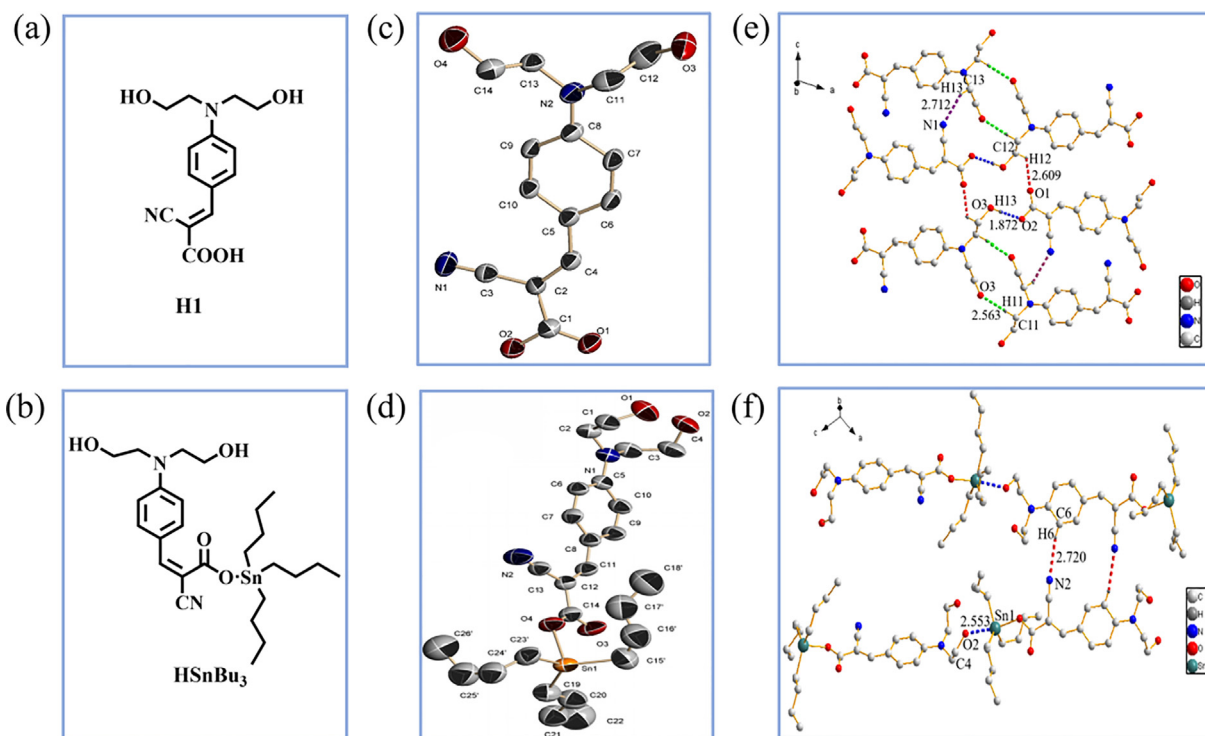
3. Results and discussion

3.1. Synthesis and characterization

Complex **HSnBu₃** was designed and synthesized through a few reaction steps. As illustrated in Fig. 1, tributyltin oxide was used to synthesize organotin (IV) complex (**HSnBu₃**) based on carboxylate ligand. The yield is 70%. All the compounds were fully characterized by ESI-MS/MALDI-TOF, ¹H and ¹³C NMR (Fig. S1–6). **HSnBu₃** has only one position of tin in ¹¹⁹Sn NMR spectra, and the chemical shift points are -25.21 ppm, indicating that **HSnBu₃** shows only mono coordination mode (Fig. S7) [31]. For reference, the chemical shift of ¹¹⁹Sn from Sn = 200 ppm to Sn = -60 ppm indicates a four coordination [32]. In addition, from the above dates of ¹¹⁹Sn NMR spectra, the complex (**HSnBu₃**) is a quaternary coordination model, which is also confirmed by the single crystal structure obtained.

3.2. Crystal structures

Single crystals of **H1** and **HSnBu₃** were slowly prepared from the ethanol system at room temperature and were characterized crystallographically (Fig. 2a–d). Both of **H1** and **HSnBu₃** crystallize in the crystal system with the P2₁/C space group (Table. S1). There are four coordinated bonds around a central Sn atom in **HSnBu₃**, namely, three Sn–C bonds and one Sn–O bond. The carboxyl C–O bond length of **H1** and **HSnBu₃** are 1.313 and 1.276 Å (**H1** > **HSnBu₃**), respectively, indicating that the carboxyl group is coordinated with Sn, and the C–O bond length of the complex is significantly shorter than that of the ligand. In addition, the distance of Sn–O is 2.152 Å, which is much smaller than the classical

Fig. 1. Synthetic routes of **HSnBu₃**.Fig. 2. Molecular structures of **H1** (a-b) and **HSnBu₃** (c,d) (All H atoms are omitted for clarity). The 1D linear chain of **H1** (e) and **HSnBu₃** (f). Single-crystal structures were present with 50% probability displacement ellipsoids.

Sn–O covalent bond of 2.80 Å, indicating that there is a strong weak force between tin atom and carboxyl oxygen atom (Table. S2-3).

As shown in Fig. 2e and f, the 1D chain of **H1** is restricted by the abundant C–H...N hydrogen bonds (d = 2.712 Å), C–H...O hydrogen bonds (d = 2.563 Å) and O–H...O hydrogen bonds (d = 1.872 Å).

Å). And for **HSnBu₃**, the existence of Sn-O bonds ($d = 2.553 \text{ \AA}$) elaborated that a flow of electrons in the center of the metal.

3.3. Optical properties

After confirming the structures of **H1** and **HSnBu₃**, we investigated their photo-physical properties through experiment and theoretical calculations. The optimization was performed on B3LYP Genecp by using the crystal structure without any symmetry restraints, and the TD-DFT {B3LYP Genecp} calculations were carried out with optimized structure [33–34]. All calculations, including optimization and TD-DFT, were performed using the G09 software. Geometry optimization of singlet–singlet excitation energies were carried out with a basis set composed of sto-3 g for C N O H atoms, and the LANL2DZ basis set for Sn atoms. The lowest 25 spin-allowed singlet–singlet transitions were taken into account in the calculation of the absorption spectra. The UV–vis absorption spectra and fluorescence spectra of **H1** and **HSnBu₃** were shown in Fig. S8, it can be found that the position and width of the absorption band are slightly different in different solvents. In DMSO, **H1** showed a strong absorption in the range of 370–430 nm, while **HSnBu₃** had an absorption wavelength in the range of 370–390 nm, which was further confirmed by TD-DFT. As shown in Fig. S9 and Table. S5, for **H1** in DMSO, the calculated peak position of the maximum absorption band is 390.95 nm, which belongs to HOMO to LUMO transition. The HOMO orbital electrons are mainly localized on the aniline group, the LUMO orbital electrons are located on the carboxyl group, indicating that the electronic transition is mainly transferred from aniline group to the the carboxyl group. for **HSnBu₃** in DMSO, the calculated peak position of the maximum absorption band is 369.57 nm, which belongs to HOMO to LUMO transition. For **HSnBu₃** in DMSO, the HOMO is mainly concentrated in the aniline group, and the LUMO is mainly located on the carboxyl group.

3.4. Two-photon absorption and fluorescence properties

In Fig. S10, we present 2PA spectra of complexes in DMSO with a concentration of 10^{-3} M . The two-photon absorption properties were presented via open aperture Z-scan curves. As shown in the Fig. 3a, both the ligand and the complex exhibit two-photon absorption activity at 900 nm (Table. S6). Taking advantage of the absorption of all compounds, the 2PEF spectra of **H1** and complex (**HSnBu₃**) in DMSO were obtained from 700 nm to 900 nm. Unfortunately, complex (**HSnBu₃**) showed weak two-photon fluorescence signals compared with ligand (**H1**) (Fig. S10 and 3b). And as observed from Fig. 3c, using fluorescein as a reference, we measured the two-photon emission intensity and calculated the two-photon absorption cross section of the complex for **H1** and complex (**HSnBu₃**). The maximum 2PA action cross sections are 8.77 GM for **H1**, 4.01 GM for **HSnBu₃**, respectively (Table. S7). The 2PA action cross section values of **HSnBu₃** are smaller than the ligand on account of the heavy atom effect of the tin atom in DMSO [35]. Importantly, the Φ_{max} for the two compounds in the NIR range (about 840 nm), which is favor of biological imaging applications due to the lower optical damaging.

3.5. Three-photon absorption and fluorescence properties

The three-photon absorption properties were presented via open aperture Z-scan curves. Interestingly, as showed in Fig. 3d and Table. S8, **HSnBu₃** exhibits excellent three-photon absorption activity at 1500 nm, and its three-photon absorption cross section is $2.12 \times 10^{-77} \text{ cm}^6\text{s}^2\text{photon}^{-2}$. However, the three-photon absorption property of the ligand is not detected at 1500 nm. In Fig. 3e, the three-photon emission intensity of **HSnBu₃** were investigated from 1150 nm to 1500 nm in DMSO. By fitting the profile with

the linear formula of $y = kx + b$, the slope of **HSnBu₃** was 2.79, indicating its three-photon fluorescence properties (Fig. S11). Using rhodamine 6G as a reference, we calculated the three-photon absorption cross section of **HSnBu₃**. And as shown in Fig. 3f, the absorption cross section of **HSnBu₃** is $2.44 \times 10^{-82} \text{ cm}^6\text{s}^2\text{photon}^{-2}$ at 1500 nm (Table. S9) and its three-photon absorption cross section is 122 times that of moxifloxacin [36], which makes it has potential in the field of three-photon fluorescence imaging.

3.6. Single and two-photon fluorescence imaging in zebra fish model

Although we have studied the two-photon and three-photon properties of the moleculars systematically, due to the limitations of the three-photon fluorescence imaging, we performed imaging studies on zebra fish only using two-photon fluorescence imaging technology. Compared with traditional single-photon absorption, two-photon absorption (2PA) has the advantage of deep penetration, which is especially beneficial for biological imaging *in vivo*. As shown in Fig. 4a, we choose 5-day-old zebra fish as the model, after feeding the **H1** and **HSnBu₃**, the confocal images of head were captured. The probes can quickly enter the organism and show strong fluorescent signals. What's more, in Fig. 4b, we can clearly see the eye of zebra fish after incubation with **HSnBu₃**, and two-photon fluorescence is obviously stronger than single-photon (Fig. 4c) [37]. The results demonstrated that **HSnBu₃** can be used for two-photon bio-imaging.

3.7. Studies on reactive oxygen species (ROS) levels and types

Due to the influence of heavy atoms in the complex, its fluorescence property is weaker than that of the ligand, we used chemical methods to detect the ROS production levels of the probe under light induction, so as to explore the potential of this probe for photodynamic therapy. 2', 7' -dichlorodihydrofluorescein diacetate ($\text{H}_2\text{DCF-DA}$), as ROS indicator, by lighting-on signal when react with ROS, was used to detect ROS generation levels of **H1** and **HSnBu₃**. After mix $\text{H}_2\text{DCF-DA}$ with probes, upon illumination, the signal of $\text{H}_2\text{DCF-DA}$ at 525 nm increased significantly, which showed that **H1** and **HSnBu₃** could produce effective reactive oxygen species (ROS) (Fig. S12) [38]. And after 80 s of irradiation, the fluorescence ratio intensity of **HSnBu₃** was 1.78 times higher than **H1** (Fig. 5a). It showed that **HSnBu₃** has a stronger ability to produce reactive oxygen species than **H1**. Next, we carried out electron spin resonance (ESR) spectroscopy to detect and analyze the types of reactive oxygen species. 5, 5-dimethyl-1-pyrroline-N-oxide (DMPO) and 2, 2, 6, 6-tetramethylpiperidine (TEMP) as the $\text{O}_2^{\bullet-}$ and $^1\text{O}_2$ trapping agents, respectively. Unfortunately, as shown in Figs. S12 and 5b, after irradiation the solution of **H1** and complex (**HSnBu₃**) with DMPO, the signal of $\text{O}_2^{\bullet-}$ was not detected [39]. Significantly, in Fig. S13 and 5c, **H1** and complex (**HSnBu₃**) can be found a characteristic triplet of signals with a relative intensity of 1:1:1 between 3410 and 3450 G after irradiation, indicating that $^1\text{O}_2$ were produced by complex (**HSnBu₃**) under light irradiation. Obviously, complex (**HSnBu₃**) can generate $^1\text{O}_2$ better than ligand (**H1**). Taking into account that complex can produce more singlet oxygen after irradiation, we have also calculated and compared the yield of $^1\text{O}_2$. ABDA is a commercial $^1\text{O}_2$ detection agent, which can selectively react with $^1\text{O}_2$ and cause a corresponding drop in absorbance. It is worth noting that the absorbance of ABDA in the **HSnBu₃** solution decreases significantly under white light irradiation (Fig. S12). Frankly, as quantitatively showed in the decomposition rate diagram of ABDA (Fig. 5d), the $^1\text{O}_2$ generation efficiency of **HSnBu₃** is 3.98 times that of **H1** [40]. Using Rose Bengal (RB) as the standard ($\Phi = 75\%$ in water), the $^1\text{O}_2$ quantum yields (Φ) of **H1** and **HSnBu₃** have been calculated to be 6.67% and 39.2% in water [41]. The above results show that **HSnBu₃** can produce more $^1\text{O}_2$ than **H1** after irradiation. Therefore, **HSnBu₃** may be as an excellent antitumor photosensitizer used in photodynamic therapy.

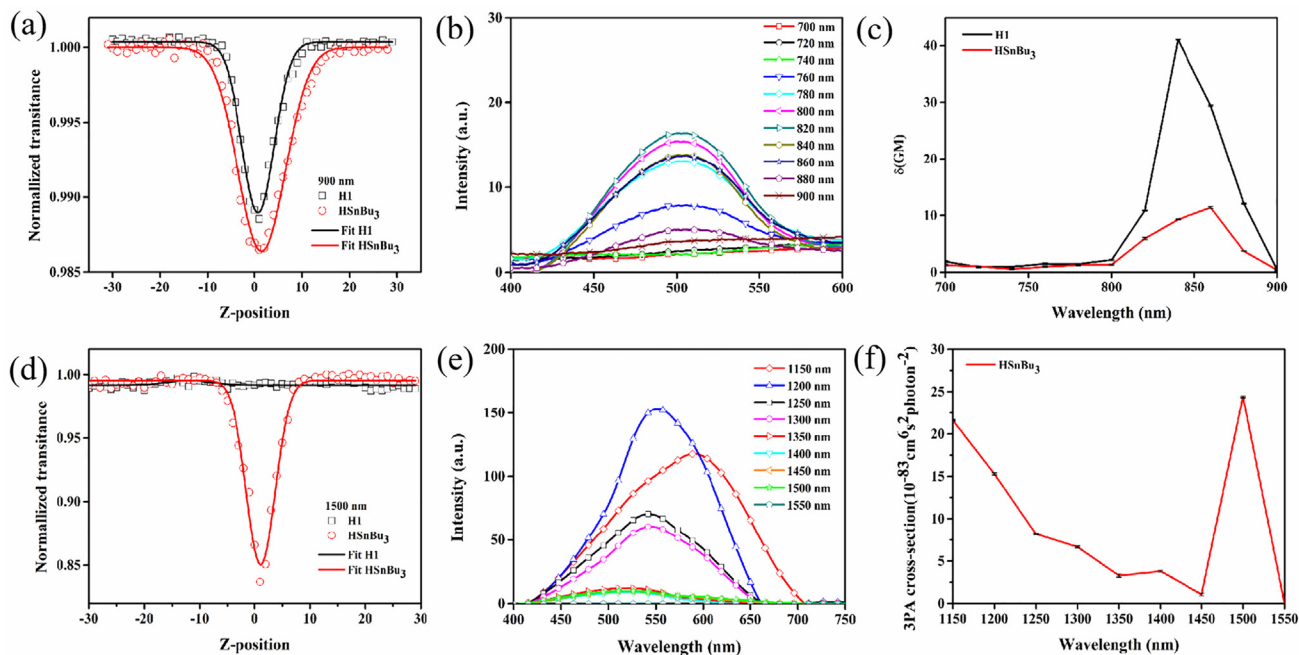


Fig. 3. (a) Two-photon absorption spectra of **H1** and **HSnBu₃** ($c = 1.0$ mM) at 900 nm in DMSO obtained through an open aperture Z-scan. (b) Two-photon fluorescence spectra of **HSnBu₃** ($c = 1.0$ mM) in DMSO with different excitation wavelength (700–900 nm). (c) Changes in two-photon absorption action cross-sections of **H1** and **HSnBu₃** ($c = 1.0$ mM) in DMSO. (d) Three-photon absorption spectra of **H1** and **HSnBu₃** ($c = 1.0$ mM) at 1500 nm in DMSO obtained through an open aperture Z-scan. (e) Three-photon fluorescence spectra of **HSnBu₃** ($c = 1.0$ mM) in DMSO with different excitation wavelength. (f) Changes in three-photon absorption action cross-sections of **HSnBu₃** ($c = 1.0$ mM) in DMSO.

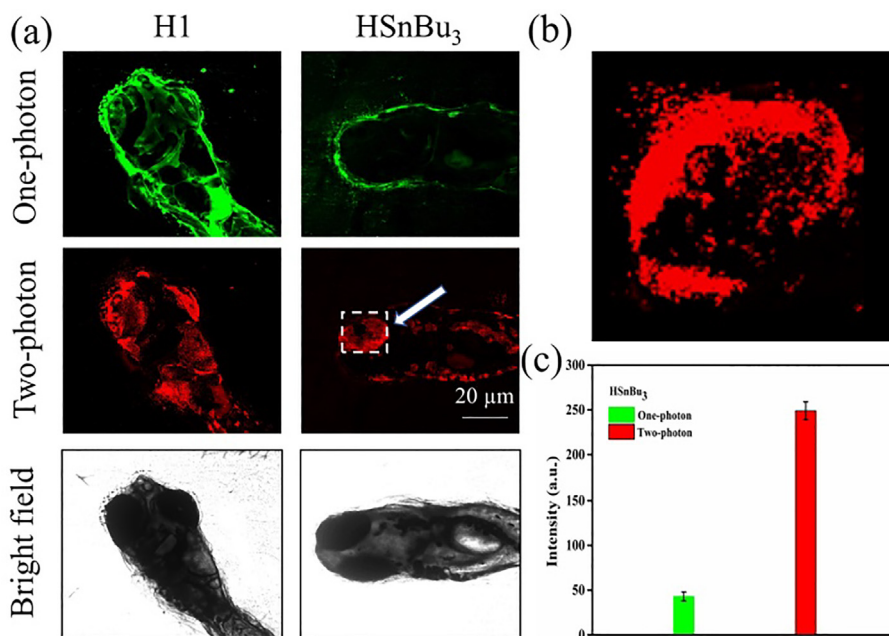


Fig. 4. (a) One- and two-photon fluorescence images of 5-day-old zebrafish incubated with **H1** and **HSnBu₃**, ($c = 30$ μ M) after 4 h of incubation, washed by PBS buffer. Excited wavelength (1P): 405 nm; emission filter: 425–525 nm. Excited wavelength (2P): 820 nm; emission filter: 425–525 nm. (b) Local two-photon imaging of zebrafish eyes after being incubated by **HSnBu₃**. (c) Diagram of relative emission intensity of single-photon and two-photon of zebrafish eyes after being incubated by **HSnBu₃**. Scale Bar: 20 μ m.

3.8. Biological application

The above results motivated us to explore the levels of ROS induced by probe photoinduced in cells, we used 2', 7' - Dichlorodihydrofluorescein diacetate (H₂DCF-DA) as an indicator. As shown in Fig. 6a, compared with the control group, the fluores-

cence signal of HepG2 cells incubated with complex (**HSnBu₃**) was significantly increased, which is consistent with the chemical test results. Mitochondria are the main pro-apoptotic targets of excess ROS. Therefore, we use the JC-1 kit to detect the mitochondrial membrane potential (MMP) to determine the cell state. In Fig. 6b, after HepG2 cells are incubated with the complex

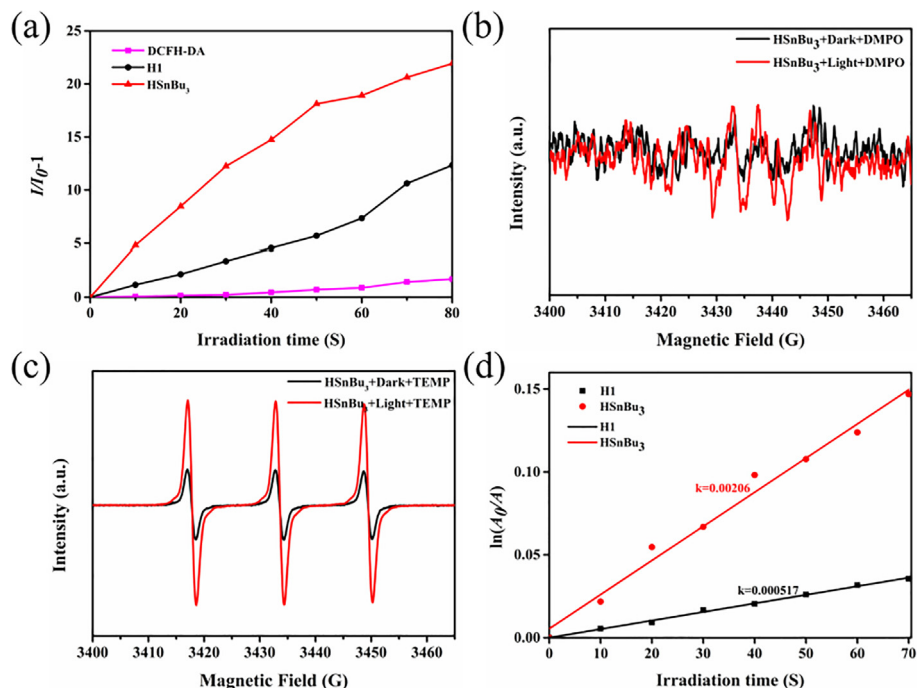


Fig. 5. (a) ROS generation in the present of **H1** and **HSnBu₃** ($c = 10 \mu\text{M}$) upon 525 nm laser irradiation. (b) ESR signals of **HSnBu₃** trapped by DMPO with times. (c) ESR signals of **HSnBu₃** trapped by TEMP with times. (d) Absorbance of ABDA ($c = 10 \mu\text{M}$) aqueous solutions at 379 nm in the present of **H1** and **HSnBu₃** ($c = 10 \mu\text{M}$) for different durations of irradiation with white light (300–800 nm, 4 mW cm^{-2}).

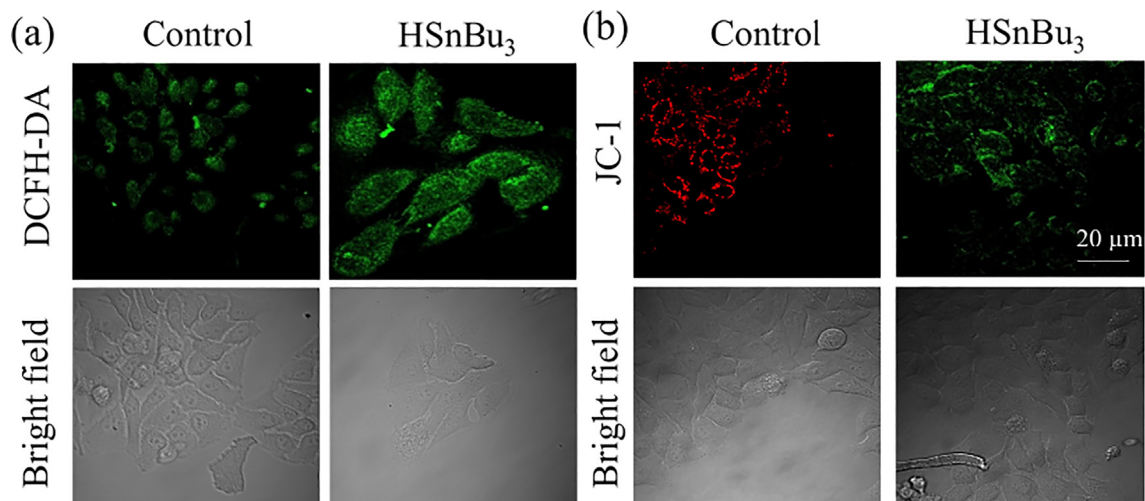


Fig. 6. (a) Fluorescence images of ROS levels in HepG2 cells after 5 h incubation with complex **HSnBu₃** ($c = 10 \mu\text{M}$), followed by DCFH-DA ($\lambda_{\text{ex}} = 485 \text{ nm}$, $\lambda_{\text{em}} = 510\text{--}540 \text{ nm}$) staining for 20 min at 37 °C. (white light irradiation 20 min, 100 mW/cm^2). (b) Confocal microscopy imaging of HepG2 cells co-labelled with JC-1 dye with or without complex **HSnBu₃** ($c = 50 \mu\text{M}$), respectively. Scale Bar: 20 μm .

(**HSnBu₃**), we can clearly see that the fluorescence of JC-1 changes from red to green, which indicates a decrease in mitochondrial membrane potential [42–43]. The decrease in the membrane potential of mitochondria indicates that the probes could produce excessive ROS in the cell to kill the cancer cells under the photo-induced condition.

4. Conclusions

In summary, we have designed a new aniline-based ligand (**H1**) and its organotin (IV) complex **HSnBu₃**. The nonlinear optical properties of the two compounds were studied. Among the evaluated ligand and complex, **HSnBu₃** showed multiphoton absorption

activity, three-photon absorption cross section was $2.44 \times 10^{-82} \text{ cm}^6 \text{ s}^2 \text{ photon}^{-2}$. The ligand does not exhibit three-photon properties. The fluorescence imaging results of zebra fish showed that two-photon fluorescence imaging possess good deep tissue imaging and can stain eyes of zebra fish compared with single-photon fluorescence imaging. By using indicators ($\text{H}_2\text{DCF-DA}$ and ABDA), we tested the levels and types of reactive oxygen species. The ROS levels produced by **HSnBu₃** was 1.78 times higher than **H1**. The ESR spectra confirmed that **H1** and **HSnBu₃** can generate $^1\text{O}_2$ and the $^1\text{O}_2$ quantum yields (Φ) of **H1**, **HSnBu₃** are 6.67% and 39.2%. We also found that **HSnBu₃** can produce excessive ROS levels and induce a decrease in mitochondrial membrane potential, which shows potential in photodynamic therapy.

Declaration of Competing Interest

The authors declare that they have no known competing financial interests or personal relationships that could have appeared to influence the work reported in this paper.

Acknowledgments

This work was supported by the National Natural Science Foundation of China (21871003, 51672002, 21701160, 21602003, 21673003 and 51772002), Start-up Grant from Anhui University for financial support (S020118002/073, S020118002/026), Nature Science Foundation of Anhui Province (1908085 MB30, 2008085QB52), National Major Scientific Instrument and Equipment Development Project (No. 21927814)

Appendix A. Supplementary material

Supplementary data to this article can be found online at <https://doi.org/10.1016/j.saa.2021.119923>.

References

- [1] I.E.H. Elhussin, S. Zhang, J. Liu, D. Li, Q. Zhang, S. Li, X. Tian, J. Wu, Y. Tian, A novel water-soluble quinoline-indole derivative as three-photon fluorescent probe for identifying nucleolus RNA and mitochondrial DNA, *Chem. Commun.* 56 (2020) 1859–1862.
- [2] A.V. Kazak, M.A. Marchenkova, K.S. Khorkov, D.A. Kochuev, A.V. Rogachev, I.V. Kholodkov, N.V. Usol'tseva, M.S. Savelyev, A. YuTolbini, Ultrathin Langmuir-Schaefer films of slipped-cofacial J-type phthalocyanine dimer: Supramolecular organization, UV/Vis/NIR study and nonlinear absorbance of femtosecond laser radiation, *Appl. Surf. Sci.* 545 (2021) 148993.
- [3] M. Zhu, G. Zhang, C. Li, M.P. Aldred, E. Chang, R.A. Drezek, A.D.Q. Li, Reversible two-photon photoswitching and two-photon imaging of immunofunctionalized nanoparticles targeted to cancer cells, *J. Am. Chem. Soc.* 133 (2011) 365–372.
- [4] M.L. Odyniec, S.J. Park, J.E. Gardiner, E.C. Webb, A.C. Sedgwick, J. Yoon, S.D. Bull, H.M. Kim, T.D. James, A fluorescent ESIPt-based benzimidazole platform for the ratiometric two-photon imaging of ONO⁻ in vitro and ex vivo, *Chem. Sci.* 11 (2020) 7329–7334.
- [5] J. Yang, B. Zhu, W. Yin, Z. Han, C. Zheng, P. Wang, C. Ran, Differentiating A β 40 and A β 42 in amyloid plaques with a small molecule fluorescence probe, *Chem. Sci.* 11 (2020) 5238–5245.
- [6] K.E. Sapsford, L. Berti, I.L. Medintz, Materials for fluorescence resonance energy transfer analysis: beyond traditional donor–acceptor combinations, *Angew. Chem. Int. Ed.* 45 (2006) 4562–4588.
- [7] C. Fang, H. Cao, C. Cai, Q. Zhang, D. Li, X. Tian, S. Li, J. Wu, Y. Tian, A three-photon probe for highly selective and sensitive detection of Ag⁺ bearing an AIE fluorophore, *Sens. Actuat. B* 325 (2020) 128820.
- [8] W. Qin, N. Alifu, J.W.Y. Lam, Y. Cui, H. Su, G. Liang, J. Qian, B. Tang, Facile synthesis of efficient luminogens with AIE features for three-photon fluorescence imaging of the brain through the intact skull, *Adv. Mater.* 32 (2020) 2000364.
- [9] Y. Wang, M. Chen, N. Alifu, S. Li, W. Qin, A. Qin, B. Tang, J. Qian, Aggregation-induced emission luminogen with deep-red emission for through-skull three-photon fluorescence imaging of mouse, *ACS Nano* 11 (2017) 10452–10461.
- [10] X. Li, J. Liu, D. Li, D. Liu, X. Tian, Q. Zhang, S. Li, J. Wu, Y. Tian, Subcellular discriminated distribution under diverse apoptosis phase using a two-photon active probe with indole moiety, *Dyes Pigm.* 184 (2021) 108790.
- [11] W. Liu, Y. Wang, X. Han, P. Lu, L. Zhu, C. Sun, J. Qian, S. He, Fluorescence resonance energy transfer (FRET) based nanoparticles composed of AIE luminogens and NIR dyes with enhanced three-photon nearinfrared emission for in vivo brain angiography, *Nanoscale* 10 (2018) 10025–10032.
- [12] C.T. Arranja, A. Aguiar, T. Encarnação, S.M. Fonseca, L.L.G. Justino, R.A.E. Castro, A. Benniston, A. Harriman, H.D. Burrows, A.J.F.N. Sobral, Double-tailed long chain BODIPYs – Synthesis, characterization and preliminary studies on their use as lipid fluorescence probes, *J. Mol. Struct.* 1146 (2017) 62–69.
- [13] P. Labra-Vázquez, R. Flores-Cruz, A. Galindo-Hernández, J. Cabrera-González, C. Guzmán-Cedillo, A. Jiménez-Sánchez, P. G. Lacroix, R. Santillan, N. Farfán, R. Núñez, Tuning the Cell Uptake and Subcellular Distribution in BODIPY–Carboranyl Dyads: An Experimental and Theoretical Study, *Chem. Eur. J.* 26 (2020) 16530–16540.
- [14] Y. Goh, H. Song, G. Lee, H. Bae, M.K. Mahata, K.T. Lee, Cellular uptake efficiency of nanoparticles investigated by three-dimensional imaging, *Chem. Chem. Phys.* 20 (2018) 11359–11368.
- [15] M.K. Mahata, K.T. Lee, Development of near-infrared sensitized core–shell–shell upconverting nanoparticles as pH-responsive probes, *Nanoscale Adv.* 1 (2019) 2372–2381.
- [16] F. Schlütter, A. Wild, A. Winter, M.D. Hager, A. Baumgaertel, C. Friebe, U.S. Schubert, Synthesis and characterization of new self-assembled metallo-polymers containing electron-withdrawing and electron-donating bis(terpyridine) Zinc (II) moieties *Macromolecules* 43 (2010) 2759–2771.
- [17] Q. Zhang, X. Lu, H. Cao, H. Wang, T. Zhu, X. Tian, D. Li, H. Zhou, J. Wu, Y. Tian, Multiphoton absorption Iridium (III)–Organotin (IV) dimetal complex with AIE behavior for both sensitive detection of tyrosine and antibacterial activity, *ACS. Appl. Bio. Mater.* 3 (2020) 8105–8112.
- [18] T. He, Y. Gao, R. Chen, L. Ma, D. Rajwar, Y. Wang, A.C. Grimsdale, H. Sun, Multiphoton harvesting in an angular carbazole-containing Zn (II)-coordinated random copolymer mediated by twisted intramolecular charge transfer state, *Macromolecules* 47 (2014) 1316–1324.
- [19] Z. Feng, D. Li, M. Zhang, T. Shao, Y. Shen, X. Tian, Q. Zhang, S. Li, J. Wu, Y. Tian, Enhanced three-photon activity triggered by the AIE behaviour of a novel terpyridine-based Zn (II) complex bearing a thiophene bridge, *Chem. Sci.* 201 (2019) 7228–7232.
- [20] X. Zhao, J. Liu, H. Wang, Y. Zou, S. Li, S. Zhang, H. Zhou, J. Wu, Y. Tian, Synthesis, crystal structures and two-photon absorption properties of triphenylamine cyanoacetic acid derivative and its organooxotin complexes *Dalton, Trans.* 44 (2015) 701–709.
- [21] H. Wang, L. Hu, W. Du, X. Tian, Q. Zhang, Z. Hu, L. Luo, H. Zhou, J. Wu, Y. Tian, Two-photon active organotin (IV) carboxylate complexes for visualization of anti-cancer action, *ACS. Biomater. Sci. Eng.* 3 (2017) 836–842.
- [22] H. Ullah, V. Previtali, H.B. Mihigo, B. Twamley, M.K. Rauf, F. Javed, A. Waseem, R.J. Baker, I. Rozasc, Structure-activity relationships of new Organotin (IV) anticancer agents and their cytotoxicity profile on HL-60, MCF-7 and HeLa human cancer cell lines, *Eur. J. Med. Chem.* 181 (2019) 111544.
- [23] M. Dahmania, A. Et-Touhami, A. Yahyi, T. Harit, D. Eddike, M. Tillard, R. Benabbes, Synthesis, characterization, X-ray structure and in vitro antifungal activity of triphenyltin complexes based on pyrazole dicarboxylic acid derivatives, *J. Mol. Struct.* 1225 (2021) 129137.
- [24] R. Guan, Z. Zhou, M. Zhang, H. Liu, W. Du, X. Tian, Q. Zhang, H. Zhou, J. Wu, Y. Tian, Organotin(IV) carboxylate complexes containing polyether oxygen chains with two-photon absorption in the near infrared region and their anticancer activity, *Dyes Pigm.* 158 (2018) 428–437.
- [25] G. Geisberger, E.B. Gyenge, D. Hinger, P. Bösiger, C. Maake, G.R. Patzke Synthesis, characterization and bioimaging of fluorescent labeled polyoxometalates, *Dalton Trans.* 42 (2013) 9914–9920.
- [26] M. Sirajuddin, S. Ali, V.N.M. Akhtar, S. Andleeb, A. Wadood, Spectroscopic characterizations, structural peculiarities, molecular docking study and evaluation of biological potential of newly designed organotin (IV) carboxylates, *J. Photochem. Photobiol. B* 197 (2019) 111516.
- [27] L. Hu, H. Wang, T. Xia, B. Fang, Y. Shen, Q. Zhang, X. Tian, H. Zhou, J. Wu, Y. Tian, Two-photon-active Organotin(IV) complexes for antibacterial function and super-resolution bacteria imaging, *Inorg. Chem.* 57 (2018) 6340–6348.
- [28] Q. Zhang, M. Zhang, H. Wang, X. Tian, W. Ma, L. Luo, J. Wu, H. Zhou, S. Li, Y. Tian, A series of two-photon absorption organotin (IV) cyano carboxylate derivatives for targeting nuclear and visualization of anticancer activities, *J. Inorg. Biochem.* 192 (2019) 1–6.
- [29] M. Zhang, W. Du, X. Tian, R. Zhang, M. Zhao, H. Zhou, Y. Ding, L. Li, J. Wu, Y. Tian, Real-time noninvasive monitoring of cell mortality using a two-photon emissive probe based on quaternary ammonium, *J. Mater. Chem. B.* 6 (2018) 4417–4421.
- [30] C. Tao, X. Han, J. Bao, Q. Chen, Y. Huang, G. Xu, Preparation of waterborne polyurethane with outstanding fluorescence properties and programmable emission intensity, *Polym Int.* 66 (2017) 770–778.
- [31] M. Sun, B. Ruan, Q. Zhang, Z. Liu, S. Li, J. Wu, B. Jin, J. Yang, S. Zhang, Y. Tian, Synthesis, crystal structures, electrochemical studies and anti-tumor activities of three polynuclear organotin (IV) carboxylates containing ferrocenyl moiety, *J. Organomet. Chem.* 696 (2011) 3180–3185.
- [32] H. Ullah, V. Previtali, H.B. Mihigo, B. Twamley, M.K. Rauf, F. Javed, A. Waseem, R.J. Baker, I. Rozas, Structure-activity relationships of new organotin (IV) anticancer agents and their cytotoxicity profile on HL-60, MCF-7 and HeLa human cancer cell lines, *Eur. J. Med. Chem.* 181 (2019) 111544.
- [33] N. Jaiswal, A.K. Kushwaha, A.P. Singh, R.K. Dubey, Synthesis, spectroscopic characterization and computational studies of Schiff base complexes of tin (IV) chloride, *Main Group Met. Chem.* 42 (2019).
- [34] O.E. Sherif, N.S. Abdel-Kader, DFT calculations, spectroscopic studies, thermal analysis and biological activity of supramolecular Schiff base complexes, *Arabian J. Chem.* 11 (2018) 700–713.
- [35] X. Zhao, J. Liu, H. Wang, Y. Zou, S. Li, S. Zhang, H. Zhou, J. Wu, Y. Tian, Synthesis, crystal structures and two-photon absorption properties of triphenylamine cyanoacetic acid derivative and its organooxotin complexes, *Dalton, Trans.* 44 (2015) 701.
- [36] S. Lee, J.H. Lee, T. Wang, W.H. Jang, Y. Yoon, B. Kim, Y.W. Jun, M.J. Kim, K.H. Kim, Three-photon tissue imaging using moxifloxacin, *Scientific. Rep.* 8 (2018) 9415.
- [37] C. Jin, F. Liang, J. Wang, L. Wang, J. Liu, X. Liao, T. Rees, B. Yuan, H. Wang, Y. Shen, Z. Pei, L. Ji, H. Chao, Rational design of cyclometalated iridium (III) complexes for three-photon phosphorescence bioimaging, *Angew. Chem. Int. Ed.* 59 (2020) 1–6.
- [38] B. Ni, H. Cao, C. Zhang, S. Li, Q. Zhang, Y. Tian, D. Li, Activated type I and type II process for two-photon promoted ROS generation: the coordinated Zn matters, *Inorg. Chem.* 59 (2020) 13671–13678.
- [39] M. Li, J. Xia, R. Tian, J. Wang, J. Fan, J. Du, S. Long, X. Song, J.W. Foley, X. Peng, Near-infrared light-initiated molecular superoxide radical generator:

- rejuvenating photodynamic therapy against hypoxic tumors, *J. Am. Chem. Soc.* 140 (2018) 14851–14859.
- [40] Y. Gao, H. Zhang, Z. He, F. Fang, C. Wang, K. Zeng, S. Gao, F. Meng, L. Luo, B. Tang, Multicationic AIEgens for unimolecular photodynamic theranostics and two-photon fluorescence bioimaging, *Mater. Chem. Front.* 4 (2020) 1623–1633.
- [41] Y. Gao, X. Wang, X. He, Z. He, X. Yang, S. Tian, F. Meng, D. Ding, L. Luo, B. Tang, A dual-functional photosensitizer for ultraefficient photodynamic therapy and synchronous anticancer efficacy monitoring, *Adv. Funct. Mater.* 29 (2019) 1902673.
- [42] H. Marlow, M.A. Tosches, R. Tomer, P.R. Steinmetz, A. Lauri, T. Larsson, D. Arendt, Larval body patterning and apical organs are conserved in animal evolution, *BMC Biol.* 12 (2014) 7.
- [43] Z. Liu, J. Zhang, Y. Sun, C. Zhu, Y. Lu, J. Wu, J. Li, H. Liu, Y. Ye, Photodynamic antitumor activity of Ru (II) complexes of imidazo-phenanthroline conjugated hydroxybenzoic acid as tumor targeting photosensitizers, *J. Mater. Chem. B.* 8 (2020) 438.